Experiments in Fluids 37 (2004) 811–824
DOI 10.1007/s00348-004-0865-4

Near-wall hindered Brownian diffusion of nanoparticles examined by three-dimensional ratiometric total internal reflection fluorescence microscopy (3-D R-TIRFM)

K. D. Kihm, A. Banerjee, C. K. Choi, T. Takagi

Abstract A three-dimensional nanoparticle tracking technique using ratiometric total internal reflection fluorescence microscopy (R-TIRFM) is presented to experimentally examine the classic theory on the near-wall hindered Brownian diffusive motion. An evanescent wave field from the total internal reflection of a 488-nm bandwidth argon-ion laser is used to provide a thin illumination field on the order of a few hundred nanometers from the wall. Fluorescence-coated polystyrene spheres of 200±20 nm diameter (specific gravity=1.05) are used as tracers and a novel ratiometric analysis of their images allows the determination of fully three-dimensional particle locations and velocities. The experimental results show good agreement with the lateral hindrance theory, but show discrepancies from the normal hindrance theory. It is conjectured that the discrepancies can be attributed to the additional hindering effects, including electrostatic and electro-osmotic interactions between the negatively charged tracer particles and the glass surface.

1 Introduction

Single molecule detection (SMD) techniques to visualize the dynamic behavior and reaction kinetics of individual molecules in living cells have recently attracted a great deal of attention (Xie 2001; Weiss 2000). The rapid development and progress of SMD techniques have ushered in a revolution in biological research. It is known that the reaction of biological molecules is generally stochastic. Thus, even if the reactions of bio-molecules are initiated at the same time, they cannot be precisely predicted without carefully tracking them (Ishijima and Yanagida 2001). However, there are certain optical issues associated with the detection and subsequent tracking of single molecules. The size of individual molecules is on the order of nanometers and they are too small to be visualized by conventional optical microscopy. To overcome this problem, bio-molecules are labeled by fluorescence dyes and visualized using fluorescence microscopy.

The non-invasive nature of the fluorophores associated with the high sensitivity and contrast has made fluorescence microscopy a prominent tool in modern cell biology (de Lange et al. 2001). However, a significant drawback of light microscopy is dictated by the laws of diffraction. The limit of resolution that can be reached by optical techniques is directly proportional to the wavelength of incident light (Hecht 2002). This diffraction limit originates from the fact that it is impossible to focus a beam of light to a spot smaller than approximately its wavelength. The challenge to break this diffraction limit has led to the development of several novel imaging techniques. One of them, total internal reflection fluorescence microscopy (TIRFM), uses an electromagnetic field called the ''evanescent field' to excite the fluorophores within several hundred nanometers from the interface (Axelrod et al. 1992). This method provides a significant improvement for near-field illumination compared to differential interference contrast (Inoue 1987), confocal microscopy (Pawley 1995, Park et al. 2004), theta microscopy (Stelzer and Lindek 1994), or multi-photon microscopy (Denk et al. 1990). TIRFM has been a popular technique for both in vitro and in vivo single-molecule detection (Ishijima and Yanagida 2001; Sako et al. 2000).

The fundamental concept of TIRFM is simple, requiring only an excitation light beam traveling at a high incident angle from the denser medium to the rarer medium (Axelrod et al. 1984). At an angle greater than the critical angle, rather than passing through and refracting in accordance with Snell's law, the beam of light is totally reflected from the glass–water interface (Hecht 2002). However, the requirements for the momentum and energy boundary conditions at the interface necessitate the existence of a very thin electromagnetic field on the order of a few hundred nanometers in the rarer medium (Goos and

Received: 20 February 2004 / Accepted: 3 August 2004
Published online: 24 September 2004

K. D. Kihm (✉), C. K. Choi
Micro/Nano-Scale Fluidics and Energy Transport (MINSFET) Laboratory, Mechanical, Aerospace and Biomedical Engineering Department, University of Tennessee, Knoxville, TN 37996-2210, USA
E-mail: kkihm@utk.edu
Tel.: +1-(865) 914-5292

A. Banerjee
Department of Mechanical Engineering, Texas A&M University, College Station, TX 77843-3123, USA

T. Takagi
Department of Electrical Engineering, Kushiro National College of Technology, Kushiro, Japan

The authors wish to thank Mr. Eiji Yokoi of Olympus America Inc. for his technical assistance in setting up the TIRFM system. The authors are grateful to the financial support sponsored partially by the NASA-Fluid Physics Research Program grant no. NAG 3–2712, and partially by the US-DOE/Argonne National Laboratory grant no. DE-FG02–04ER46101. The presented technical contents are not necessarily the representative views of NASA, US-DOE, or the Argonne National Laboratory.

Hanchen 1947). This leakage of electromagnetic field, popularly called the evanescent wave or field, undergoes exponential intensity decay with increasing distance from the surface (Born and Wolf 1980). Such a narrow and optically defined excitation depth is considered as the most effective way to overcome the background noise problem that is often the biggest problem in single-molecule imaging (Sako and Yanigida 2003).

Very recently, Zettner and Yoda (2003) proposed, seemingly, the first microfluidic application of TIRFM to measure the near-wall flow fields for a rotating Couette flow. Their TIRFM system used a prism to provide a total internal reflection and the measuring field was illuminated with a higher order evanescent wave field. The reduced illumination intensity of the higher order field and the stray rays from the multiple reflections resulted in somewhat blurry images, and, thus, an elaborate background subtraction was necessary before attempting quantifications of their images for the flow vector field. Shortly after that, the use of a special TIRF objective lens was presented to measure the Brownian motion under various flow shear conditions (Jin et al. 2003). This study is a nice example to use TIRFM for the study of near-wall particle diffusive motion. However, the measurement scope is limited to a two-dimensional in nature, similar to the former study. The out-of-plane examination of the Brownian motion will be needed to further investigate the near-wall hindered diffusion that is inherently three-dimensional.

The current paper presents a novel three-dimensional particle tracking technique development using a ratiometric TIRFM principle (Rohrbach et al. 2000; Banerjee et al. 2003) in the extremely near region to a solid surface. A three-dimensional reconstruction of the particle position is performed by combining a two-dimensional planar (x–y) tracking of the lateral movement of the particles and the ratiometric TIRFM to determine the line-of-sight (z) movement. This ratiometric technique can now be called the R-TIRFM imaging technique. A robust neural network model to track particle pairs has been also developed to simultaneously measure the three-dimensional Brownian diffusive motions of nanoparticles. The experimental findings clearly give evidence of the theory of near-wall hindered diffusion, particularly within sub-micron ranges from the solid wall surface. The measurement results are compared with the Stokes flow model for diffusion (Einstein 1905) and the hindered diffusion theories (Goldman et al. 1967; Brenner 1961; Kim and Karrila 1991). The present study is considered as the first attempt, to the authors' knowledge, to experimentally validate and examine the near-wall hindered diffusion theory fully in a three-dimensional mode[1].

[1] Hosoda et al. (1998) have shown that the near-wall Brownian motion is found to be anisotropic with respect to the directions parallel and perpendicular to the interface using evanescent wave microscopy. Spectroscopic analysis was conducted, allowing a wide range of wave number, by varying the incident ray angle, and the resulting autocorrelation function of the image intensity showed evidence of the anisotropy. However, the scope of their work is far from being comprehensive in that no quantitative measurements of the near-wall hindered diffusion motion have been conducted and compared with the existing theories.

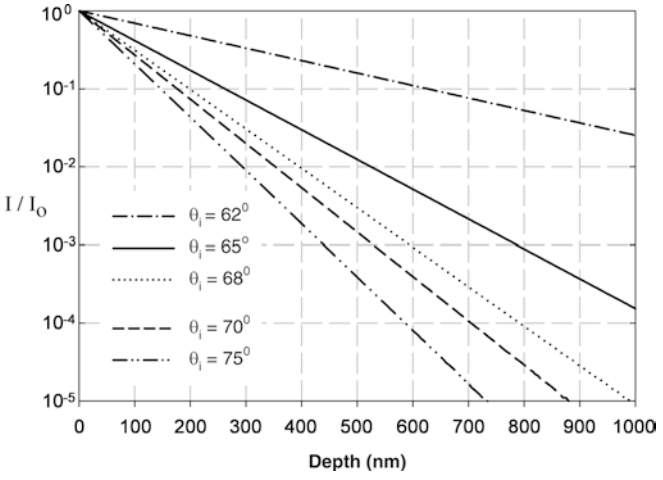

Fig. 1. Calculated evanescent wave field intensity $I(z)/I_o$ for different incident angles θ, with increasing depth z measured from the glass–water interface (n_i=1.515 for glass, n_t=1.33 for water), where the incident light intensity is I_o

2 Theoretical basis and experimental setup

2.1 Evanescent wave theory

As the ray incident angle, measured relative to the normal, increases, it reaches the *critical incident angle*, $\theta_c=\sin^{-1}(n_t/n_i)$, at which the angle of refraction is 90°. At angles larger than the critical angle, light is completely reflected at the interface, i.e., total internal reflection. This description, however, is only true from the macroscale point of view. From the microscale point of view, a portion of the incident light penetrates through the interface into the external medium, and propagates parallel to the surface in the plane of incidence, creating an electromagnetic field in the liquid (the external medium) adjacent to the interface. This field, termed as the *evanescent field*, is capable of exciting fluorophores residing in the immediate region extremely near the interface.

The evanescent wave intensity I decays exponentially with the normal distance z measured from the interface located at z=0 (Hecht 2002):

$$I(z) = I_0 \mathrm{e}^{\left(-\frac{z}{z_\mathrm{p}}\right)} \tag{1}$$

where I_0 is the incident light intensity at the interface and the penetration depth at $I/I_o=\mathrm{e}^{-1}$ is determined as:

$$z_\mathrm{p} = \frac{\lambda_0}{4\pi}\left(n_i^2 \sin^2\theta - n_t^2\right)^{-\frac{1}{2}} \tag{2}$$

Figure 1 shows the evanescent wave field intensity variation, based on Eqs. 1 and 2, with increasing depth z measured from the glass–water interface (n_i=1.515 for glass, n_t=1.33 for water) for different incident angles θ. With increasing θ, the field intensity decays faster and the penetration depth z_p is smaller[2]. Note that for all incident

[2] Refer to Fig. 10 in the Appendix for the calculation uncertainties in determining the penetration depth.

angles, 10% intensity is reached within a 300-nm range from the interface.

2.2
High numerical aperture objective-based TIRFM system

Traditionally, two different configurations of TIRFM are popular (Axelrod 1984). The first setup with a prism can be readily achieved and requires only the microscope, prism, and laser. This setup requires that the specimen be positioned between the prism and the microscope objective, and the higher order evanescent wave field must be used due to the geometrical constraint, which substantially weakens the field intensity after repeated internal reflection modes. In addition, because of the repeated reflection modes, more stray rays are rendered, resulting in images with low signal-to-noise ratios.

The second, and presently preferred, setup implements the laser to be illuminated through an inverted microscope, and greatly benefits from a special TIRF objective lens with a numerical aperture (NA) greater than 1.4. Figure 2a shows the schematic illustration of the objective-lens-based TIRFM system where an Olympus Plan APO 60X oil-immersed TIRF lens with an NA of 1.45 is used. The experimental setup consists of an inverted microscope (IX-50, Olympus Inc.), a 200-mW CW argon-ion laser (tuned at 488 nm, Laser Physics Inc.), a frame grabber board (QED Imaging Inc.), and particle tracking analysis software, which has been developed at the Micro/Nano-Scale Fluidics and Energy Transport (MINSFET) Laboratory, University of Tennessee (http://www.engr.utk.edu/~minsfet/). The upper outlet port of the microscope is connected to the CCD camera[3]. Tested nanoparticles are yellow–green (505 nm/515 nm) carboxylate-coated fluorescent micro-sphere beads[4] of 200 nm (±20-nm variance) in diameter, which have a specific gravity of 1.05 and carry weakly negative charges because of their $COOH^-$ group attached to carboxylate (Molecular Probes Inc.). The specimen is placed on the upper surface of the 170-μm thick glass slip, which is viewed from the below.

The critical angle for the lens with total internal reflection at a water–glass interface is $\theta_c=\sin^{-1}(1.33/1.515)=61.38°$. For an oil-based objective with 1.45 NA, the maximum angle of the passage of light is $\sin^{-1}(\mathrm{NA}/n_i)=\sin^{-1}(1.45/1.515)=73.15°$ (Hecht 2002). The present optical configuration allows the incident angles to be varied from $\theta_i=62°$ ($z_p=272$ nm) to 68° ($z_p=86$ nm)[5]. As schematically illustrated in Fig. 2b, the angle of incidence is determined by using a transfer function $R=fn\sin\theta_i$ involving the off-center location of the laser beam in the optical pathway of the microscope R, the focal length of the TIRFM objective f, and the refractive index n of the cover glass or, equivalently, of the index-matching oil (see first section of the Appendix for related discussions).

Figure 3 provides a comparison between the direct and the evanescent wave illuminated images. For the non-TIRFM image with $\theta_i=60°<\theta_c$ (Fig. 3a), light scattering from out of focus particles causes significant background noise. For the TIRFM image with $\theta_i=65°$, the signal-to-noise ratio is substantially improved because of the discrete illumination field specified by the penetration depth of $z_p=114$ nm (Fig. 3b).

2.3
Ratiometric TIRFM imaging analysis

The detected fluorescence signal at an arbitrary test field point (x, y) integrated in the line-of-sight direction z through the microscope objective (Fig. 4), $F(x, y; z_p)$ can be described as (Rohrbach 2000):

$$F(x, y; z_p) = \varepsilon I_0(x, y; z_p)\int_0^\infty [Q(z)P_D]C(x, y, z)e^{-\frac{z}{z_p}}dz \quad (3)$$

where ε defines the quantum efficiency of the fluorescent particles and of a CCD camera, which is assumed to be equal for all depth-wise locations z, and $I_0(x, y; z_p)$ is the illumination intensity at the coverslip glass–water interface. The integration in the z direction implies that the signal detected by a CCD camera represents the line-of-sight integrated image via the microscope objective. The presence of a dielectric interface (the coverslip in this case) significantly alters the probability of detecting the emitted fluorophores. This effect is traditionally expressed by the collection efficiency $Q(z)$ of the objective lens. The collection efficiency is defined as the collected power to the total power dissipated by a dipole, and its detailed mathematical formulations have been attempted by various authors (Burghardt and Thompson 1984; Hellen and Axelrod 1986). The detection probability P_D is set equal to 1, since it is expected to be constant over the evanescent wave field. Lastly, $C(x, y, z)$ denotes the three-dimensional fluorophore distribution, which is defined discretely as:

$$C(x, y, z) = \begin{cases} C & \text{if } \sqrt{x^2+y^2+(z-h)^2} \leqslant R \\ 0 & \text{if } \sqrt{x^2+y^2+(z-h)^2} > R \end{cases} \quad (4)$$

where R is the fluorescent particle radius.

[3] Model UP-1830 UNIQ with 1024×1024-pixel CCD elements and each pixel element is of dimension of 6.45×6.45 μm. The camera operates at 30 frames per second, with minimum illumination of 0.04 lux and a signal-to-noise ratio better than 58 dB. A certain level of image smearing because of the finite exposure time is inevitable, and this may result in the blurring of the particle image to a certain degree. However, the finite exposure time does not affect the ratiometric measurements where only the intensity ratios are analyzed and the intensity ratio is unaffected by the image blur. Note that the measured particle location is referred to its closest pole from the solid surface, i.e., the brightest point (refer to Sect. 2.3).

[4] The dye particles are believed to be free from the "photo-bleaching" effect that can render the dye unable to fluoresce after being excessively exposed to high-intensity pumping light. As per the specifications of Molecular Probes (2004), the aqueous suspension of fluorescent beads do not fade noticeably when illuminated by an intense 250-watt xenon-arc lamp for 30 min. Since the current experiment uses approximately 40-mW illumination at 488-nm bandwidth from the 200-mW nominal laser for the total exposure time of up to 4 s, any errors associated with photo-bleaching should be negligibly minimal.

[5] The high-NA objective-based TIRFM system adjusts the incident angle using a fiber optic laser guide attached to a precision positioning system traveling along the barrel axis (http://www.olympusmicro.com/primer/java/tirf/tirfalign/index.html).

After substituting Eq. 4 into Eq. 3 and then performing substantial mathematical manipulations, including a pertinent three-dimensional integration with an assumption of $Q(z)$=1.0, the normalized intensity detected by a CCD camera for a fluorescent particle of radius R located at a distance h from the interface (Fig. 4) is expressed as:

$$I_N(h,\ R,\ c) = 4\pi c z_p^3 \left[\left(\frac{R}{z_p}\right) \cosh\left(\frac{R}{z_p}\right) - \sinh\left(\frac{R}{z_p}\right) \right] e^{-\frac{h}{z_p}} \quad (5)$$

Although Eq. 5, in principle, can determine the particle location (h) by measuring I_N under a specified penetration depth (z_p), the fluorescence concentration function c is difficult to measure and usually not accurately known.

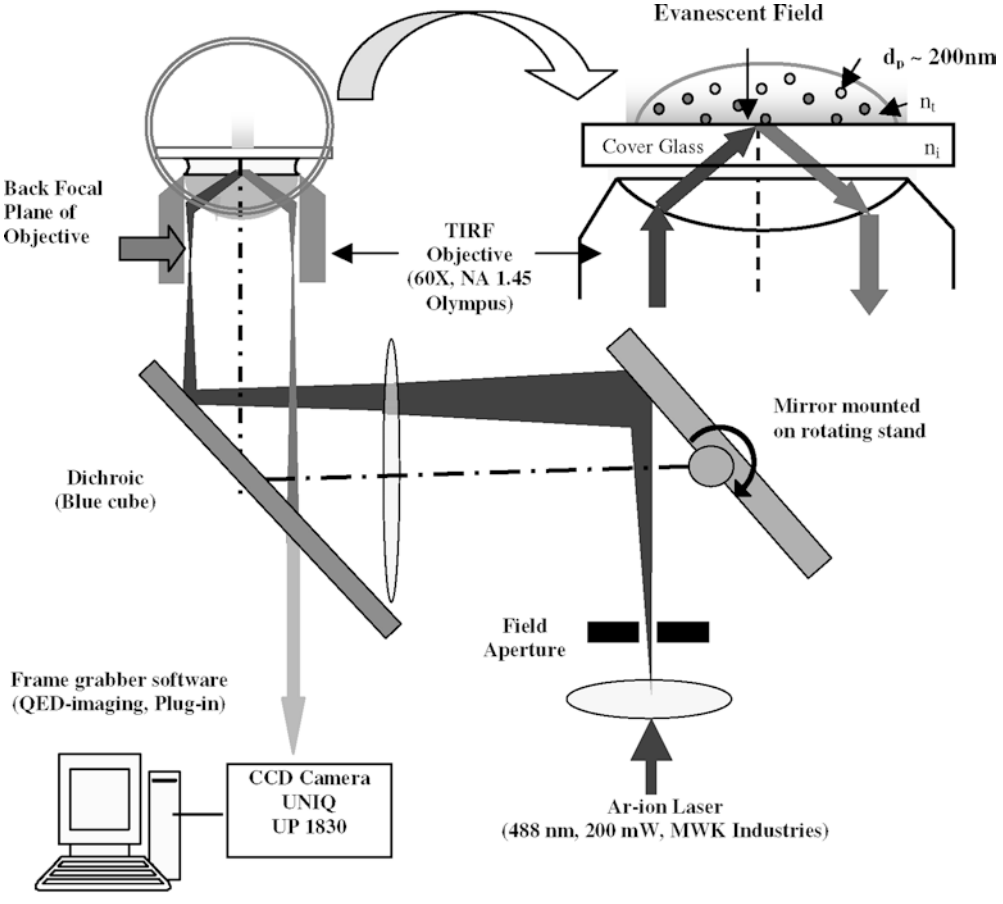

(a)

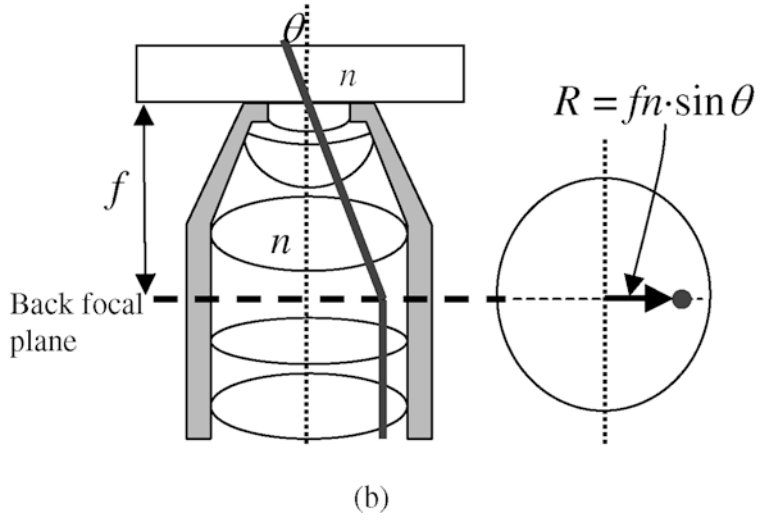

(b)

Fig. 2. a Schematic illustration of TIRFM setup with high NA (oil-immersion type) objective lens. **b** Illustration of calculation of the beam incident angle using a transfer function for the off-center laser beam location

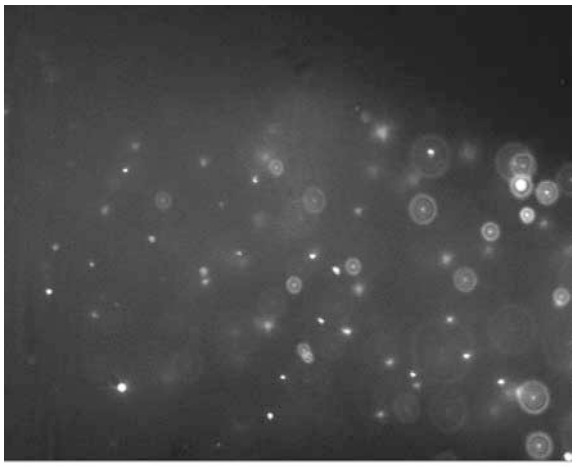

(a) Direct Illumination with $\theta_i = 60°$ ($\theta_{critical} = 61.38°$)

(b) Near Wall TIRFM Image with $\theta_i = 65°$ ($z_p = 114$ nm)

Fig. 3a, b. Comparison of direct illuminated image at an incident angle slightly below the critical angle (**a**), and evanescent wave illuminated image with an incident angle larger than the critical angle (**b**)

By taking the quotient of two recordings, the unknown fluorophore concentration c can be eliminated. Thus, by taking the ratio of I_N from two different particles at two different z locations, the determination of their relative locations is more appropriate in that the unknown and other experimental uncertainties are cancelled out, i.e.:

$$RaInt = \frac{I_N^1(h_1,\ R,\ c)}{I_N^2(h_2,\ R,\ c)} = \mathrm{e}^{\left(-\frac{\Delta h}{z_p}\right)} \tag{6}$$

To obtain the relative position Δh of two particles from the ratiometric intensity *RaInt*, care must be taken to consider the brightest particle as the reference point[6] of z=0. The relative intensity of other particles, Eq. 6, can determine their depth-wise z locations with respect to the reference zero point. The peak (or maximum) intensity from each particle image is taken for I_N and the resulting ratio of Eq. 6 identifies the nearest point of a particle from the surface.

[6] The physical location of the brightest particle may not be exactly at zero at the solid surface; rather, it should be at the most probable separation distance. Since both the glass surface and the particles are negatively charged, there exists the most probable separation distance, which is equivalent to the minimum potential energy state ensuring the mechanical equilibrium. Thus, z=0 here indicates just a reference point for the relative locations of other less bright particles.

2.4 Free and hindered Brownian diffusive motions

The observation of random motion was first reported by Jan Ingenhousz (1779) and was subsequently rediscovered and named after the eminent botanist Robert Brown, who noted the random motion of pollen particles under a microscope (1828). Albert Einstein used the kinetic theory to derive the diffusion coefficient for such motion in terms of fundamental parameters of the particles and liquid for his well-known doctoral dissertation published in 1905. The classical theory of Einstein applies to suspensions, which are effectively so dilute that each particle is moving alone in an infinite fluid. The particle can be assumed to be a sphere that is large compared to the molecules of the fluid (solvent). Thus, the frictional resistance of the particle can be calculated, taking into consideration ordinary particle hydrodynamics, i.e., given by Stokes Law as:

$$F_\mathrm{d} = 3\pi\mu d_\mathrm{p} u_\mathrm{d} \tag{7}$$

and the diffusion coefficient D for a dilute suspension of particles, originally defined by Einstein (1905, 1956) as:

$$D = \frac{kT}{3\pi\mu d_\mathrm{p}} \tag{8}$$

where k is the Boltzman constant (1.3805×10^{-23} J/K), T is the absolute temperature, and μ is the dynamic viscosity of the fluid. Recently, using a simple video microscopy (Salmon et al. 2002; Nakroshis et al. 2003), the elementary one- and two-dimensional Brownian motions have been examined for freely diffusing 1.02-μm polystyrene spheres suspended in water to show the validity of the Einstein relationship and inversely determine the Boltzman constant.

Being stochastic in nature, the mathematics of Brownian motion is actually deep and subtle, and care should be taken to interpret the results. It should be kept in mind that a diffusion equation does not provide information on the particle trajectory (Shlesinger et al. 1999). Various authors have erred in attempting to define a constant velocity v for the Brownian trajectory by taking the limit $\Delta x/\Delta t$ for a small displacement Δx and a small time Δt. The proper limit involves forming the diffusion coefficient $D=(\Delta x)^2/\Delta t$ as both Δx and Δt tend to zero. Thus, for a finite time interval, the parameter to be used for defining a random walk pattern should be the mean square displacement (MSD), rather than a misleadingly incorrect attempt to convert the definition of D into a physically groundless "Brownian velocity" as $\sqrt{D/\Delta t}$ or its multiplication by a constant.

A three-dimensional MSD is referred to random thermal or Brownian diffusivity by the Einstein–Smoluchowski equation as:

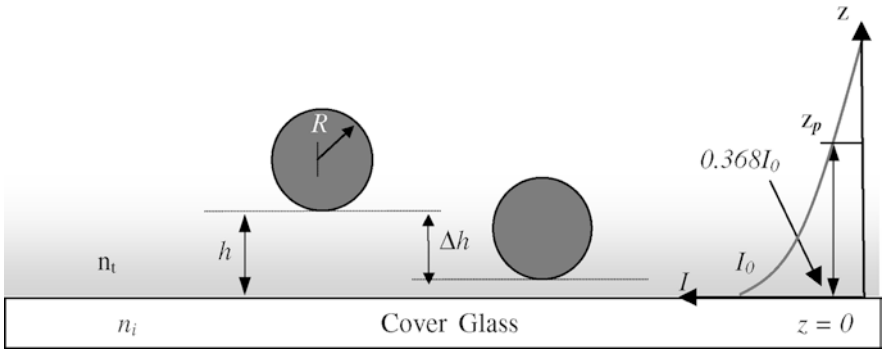

Fig. 4. Two nanoparticles at different z locations schematically illustrating the R-TIRFM imaging analysis technique

$$\langle \Delta r^2 \rangle = \langle \Delta x^2 \rangle + \langle \Delta y^2 \rangle + \langle \Delta z^2 \rangle = 6D\Delta t \tag{9}$$

where Δt is the time interval for the Brownian process and the operator $\langle \cdot \rangle$ denotes an averaged MSD. For example, $\langle \Delta r^2 \rangle = \frac{\sum_i^N \Delta r_i^2}{N}$ and $\langle \Delta y^2 \rangle = \frac{\sum_i^N \Delta y_i^2}{N}$ for three-dimensional MSD and y-directional (one-dimensional) MSD, respectively. Note that the mean displacement $\langle \Delta r \rangle$ of the particle vanishes because of the spherical symmetry of random motion and because it contains no information on D (Deen 1998).

When the particle is present close to a solid wall, the particle hydrodynamics changes significantly. Stokes law applies only to a fluid medium that extends to infinity in all directions. This assumption does not strictly hold true as a free surface or a rigid wall forms an external bound to the fluid. Furthermore, it has been found that the dynamics of the particles close to the wall become significantly non-Gaussian and the average particle displacement differs from the theoretically predicted most probable particle displacement (Schatzel et al. 1992).

The presence of these boundaries at finite distances from the particle necessitates the corrections to the Stokes resistance formula. Brenner (1961) provided an analytical expression in the form of an infinite series for this correction term. He used a hypothesis of no relative motion at the fluid–solid interface. By using an analogy of evanescence of velocity at the plane wall, Brenner refined his boundary conditions and solved the resulting Navier–Stokes equation for a creeping flow to derive the correction parameter ξ for the correction of the diffusion coefficient in the normal direction as:

$$\xi^{-1} = \frac{4}{3}\sinh\alpha \sum_{n=1}^{\infty} \frac{n(n+1)}{(2n-1)(2n+3)} \times \left[\frac{2\sinh(2n+1)\alpha + (2n+1)\sinh 2\alpha}{4\sinh^2\left(n+\frac{1}{2}\right)\alpha - (2n+1)^2\sinh^2\alpha} - 1 \right] \tag{10}$$

where α is given as a function of the particle diameter d_p and the elevation h from the interface to the base (the bottom most point) of the sphere:

$$\alpha = \cosh^{-1}\left(\frac{2h + d_p}{d_p}\right) \tag{11}$$

Now, the "hindered" one-dimensional normal diffusion coefficient $D_\perp$ of a spherical particle at a base distance h from the wall can be written as:

$$D_\perp = \xi \frac{kT}{3\pi\mu d_p} = \xi D \tag{12}$$

The findings of Brenner has been supported by a number of authors who have highlighted the need for a correction to the Stokes law for a particle close to a wall, or for the case where there are two or more particles close to each other (Dufresne et al. 2000).

Goldman et al. (1967) analyzed the slow viscous motion of the sphere parallel to a plane wall bounding a semi-infinite, quiescent, and viscous fluid, and used an asymptotic solution of the Stokes equation for rotational and translational motion close to the wall. Using an analogy corresponding to a translational lubrication theory, corrected values of the tangential forces and torques on the spherical particle have been evaluated. The resulting correction parameter for the tangential force as a result of the presence of the solid wall is given by:

$$\beta^{-1} = \left[1 - \frac{9}{16}\left(\frac{d_p}{d_p + 2h}\right) + \frac{1}{8}\left(\frac{d_p}{d_p + 2h}\right)^3 - \frac{45}{256}\left(\frac{d_p}{d_p + 2h}\right)^4 - \frac{1}{16}\left(\frac{d_p}{d_p + 2h}\right)^5 \right] \tag{13}$$

which is a function of the particle diameter d_p and its elevation h. Thus, the "hindered" tangential diffusion coefficient $D_{||}$ of a spherical particle at a distance h from the wall can be written as:

$$D_{||} = \beta \frac{kT}{3\pi\mu d_p} = \beta D \tag{14}$$

The correction factor for the three-dimensional diffusion coefficient is given as:

$$D_O = \psi D \text{ with } \psi = \frac{2\beta + \xi}{3} \tag{15}$$

where the arithmetic addition of all three directional components of the MSD constructs the total or bulk MSD as shown in Eq. 9. The values of ξ, β, and ψ for a particle diameter of 200 nm and for various elevations up to 1.0 μm, are shown in Fig. 5. When multiple particles are present, particle-to-particle interactions should be carefully examined. However, if the ratio of the separation distance to the particle radii is greater than 10, the particle interaction effects can be neglected (Batchelor 1975). Thus, inter-particle interaction is kept to a minimum in the experiment by taking a volume fraction of 0.001%.

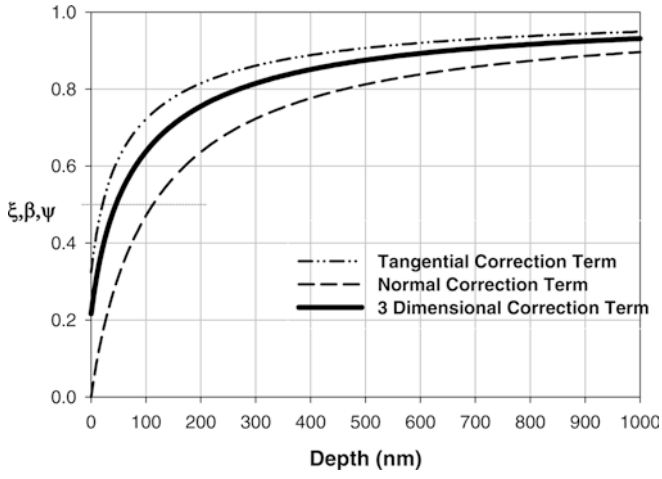

Fig. 5. Correction factors for bulk, normal (Brenner 1961), and tangential (Goldman et al. 1967) diffusion coefficients as the particle approaches the wall (d_p=200 nm)

2.5
Neural-network-based 3-D particle tracking algorithm

The novel neural network model finds the relationship among particles between a pair of images (Takagi and Okamoto 2001). The overall operation of the network model is similar to the competitive learning paradigm (Kohonen et al. 1994). A simple two-layer network model (Okamoto et al. 1995, 1997) is chosen for analysis (Fig. 6). The first layer of the network is the input layer that corresponds to the pth image. The second layer corresponds to the qth image. The two layers are fully interconnected, as seen in Fig. 6a, and the particles of the first and the second layers are labeled as $P=\{p_1, p_2,..., p_n\}$ and $Q=\{q_1, q_2,..., q_n\}$. The coordinates corresponding to the center of each particle in the first layer is (x_{pn}, y_{pn}), while in the second layer it is given as (x_{qn}, y_{qn}). The distance function between two particles of successive layers is given as:

$$d_{i,j} = \sqrt{\left(x_{pi} - x_{qj}\right)^2 + \left(y_{pi} - y_{qj}\right)^2} \tag{16}$$

where the particle center locations are identified as the centroid of the better-defined particle images after being processed using a standard 5×5-pixel Gaussian filtering.

Each interconnection in the network model carries an associated weight value (Fig. 6b) as a measure of the correspondence level between paired particles (Kohonen 1995). For each pair, the weight function w_{ij} is assigned to have a small initial value, such as 0.01, and then updated by a rule specified as:

$$w_{ij}(t+1) = w_{ij}(t) - \alpha d_{ij} w_{ij}(t) \tag{17}$$

where $w_{ij}(t)$ is the weight value between the ith particle of the first image and the jth particle of the second image, and $w_{ij}(t+1)$ is an updated weight value. The momentum coefficient α is a type of relaxation factor to control the optimization speed and accuracy, and the coefficient is usually set to be less than 1.0, mostly by trial-and-error. When the value of the weight between particles is large, the probability of the corresponding particle is high, showing optimally minimized inter-particular distance d_{ij}. Once all the normalized weight values become greater than a specified threshold, which is to be set to close to 1.0, the iteration stops and the corresponding particle image pairs are identified to provide the most probable displacement of the particle between the successive images.

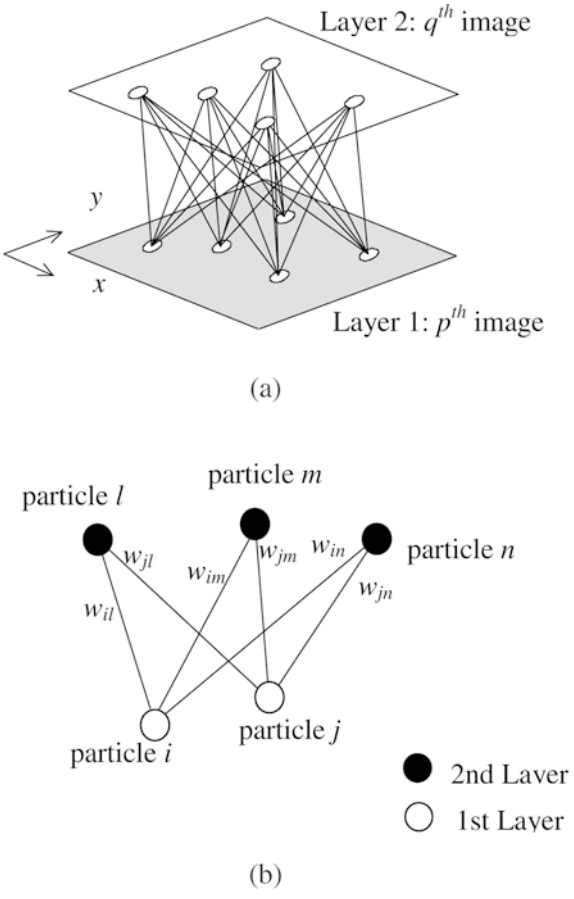

Fig. 6. Architectural illustration of the neural network model interconnecting all particles on the first image (i, j) and those on the second image (l, m, n). **a** Fully interconnected layers. **b** Weighted connections

3
Results and discussion

Results are presented for near-wall hindered Brownian diffusive motion measured two-fold: (1) manual tracking of a single particle, and (2) digital image tracking of multiple particles based on particle paring using the neural network algorithm. An incident angle of 62° is used to create an evanescent field thickness z_p of 272 nm for all the experiments. The incident angle is selected so that the penetration depth is sufficiently larger than the near-wall Brownian displacement predictions[7].

[7] For d_p=200 nm, k=1.38054×10^{-23} J/K, μ=0.001N s/m for water at T=293 K, the free Brownian diffusivity (Eq. 8) is given as D=2.1451 μm^2/s and the averaged square displacement $\langle \Delta z^2 \rangle$=2$D\Delta t$=0.142 μm^2 for the time interval of 33 ms of the 30 fps imaging. The average displacement $\langle |\Delta z| \rangle$ can be approximated to $\sqrt{\langle \Delta z^2 \rangle}$ = 377 nm. The near-wall hindered displacement (Fig. 5) will reduce it to about a half, i.e., $\langle \Delta z \rangle \sim \pm 189$ nm, which occupies approximately 70% of z_p.

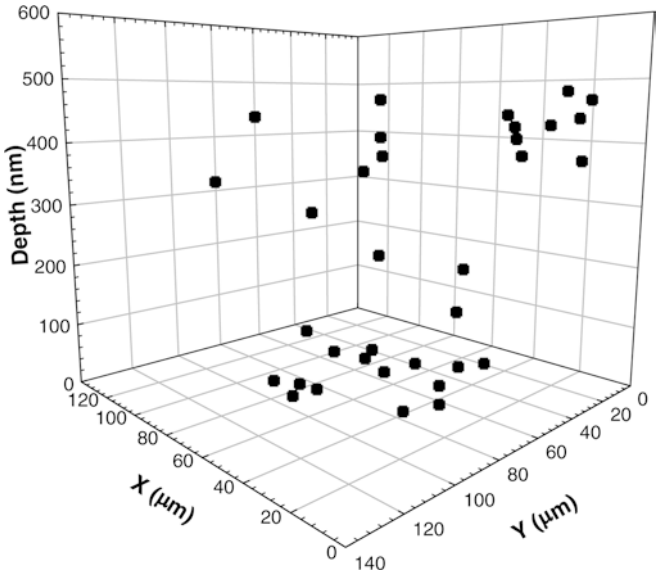

Fig. 7. Three-dimensional locations of 200-nm diameter fluorescent particles measured by R-TIRFM imaging analysis (θ_i=62°)

The test particle diameters do not have to be smaller than z_p, since only the maximum image intensity, usually corresponding to the closest pole of a particle from the solid surface, is detected and analyzed for R-TIRFM. Cell biologists, surface chemists, and colloid scientists have successfully used evanescent wave microscopy to study the motion of cells and colloids of size ranges up to 10 μm (Prieve 1999; Bevan and Prieve 2000). Rohrbach (2000) also used a 60-nm thick evanescent wave field to measure the location of a spatially fixed 300-nm particle using a similar technique. The current penetration depth of 272 nm should be fairly sufficient to illuminate the 200-nm test particles.

Figure 7 shows manually tracked results for the relative locations of multiple 200-nm particles, as frozen in a single frame, with respect to the brightest particle being the zero reference point in the line-of-sight z direction. The uncertainty of the ray angle adjustment is estimated to be ±0.315° for θ_i=62° (see first section of the Appendix). For each particle image, the maximum spot intensity is used to calculate the intensity ratio of Eq. 6 and the measured z location represents the position of the particle bottom. The measurement uncertainties for the lateral x–y locations are estimated as ±71.7 nm, which is simply equivalent to a half-pixel distance in both directions (see second section of the Appendix). The depth-wise location uncertainty decreases with increasing incident angle because of the similar dependence of the penetration depth uncertainty (see third and fourth sections of the Appendix). For the ray angle of 62°, the uncertainty of Δh in the z direction is estimated to be ±29.38 nm[8].

Figure 8 shows manually tracked results of an arbitrarily chosen single particle mapped consecutively up to 67 frames when it disappears beyond the effective visualization depth. As the distance of the particle from the interface increases, the intensity decreases exponentially until the particle vanishes totally. The particle is assumed to be beyond the effective visualization depth when the difference between its maximum pixel intensity and the surrounding pixel intensity approach within 10%. The anisotropic nature of x–y–z components shown in Fig. 8b clearly shows evidence of the anisotropic near-wall hindrance in Fig. 5. While the x and y displacement shows virtually no distinction (as they should), the significantly further reduced z displacement shows evidence of the more pronounced hindered Brownian motion in the z direction.

The pixelized data characteristics are inevitable for any CCD imaging with a discrete pixel resolution, as shown in the discretization length scales of approximately 200 nm in Fig. 8a, b. The so-called data discretization can be reduced in two ways: (1) by using a CCD camera with increased pixel resolution (for example, the use of a 2048×2048-pixel CCD camera will reduce the discretization length scale by a half from the current case of a 1024×1024-pixel CCD camera); or (2) by increasing the image magnification so that the field displacement corresponding to a single pixel can be reduced (for example, a substitution of the current 60× objective with a 100× one, the discretization will be reduced to 62.5%). The first option will be excessively costly and the second option will be more viable, but will substantially reduce the field-of-view size. Since the z location is determined based on the ratiometric principle, Eq. 6, no systematic discretization is apparent, other than the gray-level discretization of roughly 1/256, which is significantly smaller than that of the x–y displacements.

Figure 9 shows the dynamic behavior of the entire population of particles for the total of 90 frames using the neural-network-based particle tracking algorithm as described in Sect. 2.5. Figure 9a presents the lateral displacements that are anisotropic and random on the x–y plane, and Fig. 9b, c present the particle displacements on the normal x–z and y–z planes, respectively. The more pronounced reduction of particle displacements in the z direction, in comparison with the lateral displacements in the x–y plane, is persistent with the theoretical predictions of hindered diffusion in the vicinity of a wall (Fig. 5). Figure 9d presents vectors of three-dimensional displacements that are substantially quenched in the normal direction to conform to an oval shape.

Both the single-particle manual tracking data and the neural-network-based multiple particle tracking data are then compared with the theoretical predictions and the results are summarized in Table 1. The parameters compared include the MSD, mean displacements, absolute mean displacements, and elementary ($D_\perp$, $D_\parallel$), and bulk (D_O) diffusion coefficients, for 200-nm particles in water at T=293 K and for the measurement time interval of 33 ms. While the theoretical isotropic diffusion coefficient is evaluated as D=2.1451 μm^2/s, all other presented theoretical values in Table 1 represent their near-wall hindered results, as shown in Eqs. 12, 14, and 15. Spatially averaged correction coefficients within the penetration depth are used to predict theoretical values of the hindered diffusion

[8] When the ray angle increases to 65°, the uncertainty is noticeably reduced to ±6.85 nm, but its penetration depth will not be sufficient to accommodate the pertinent Brownian motion length scale.

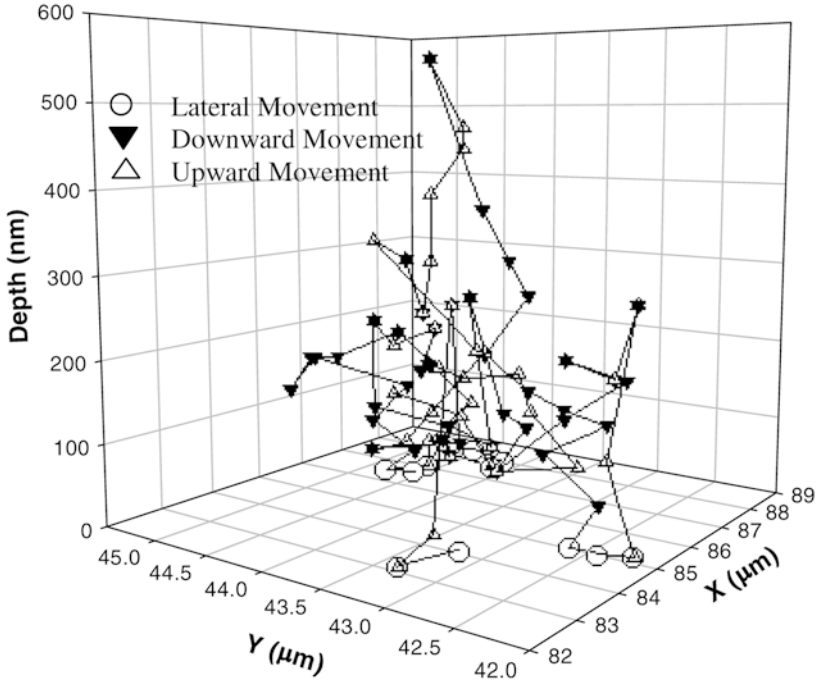

(a)

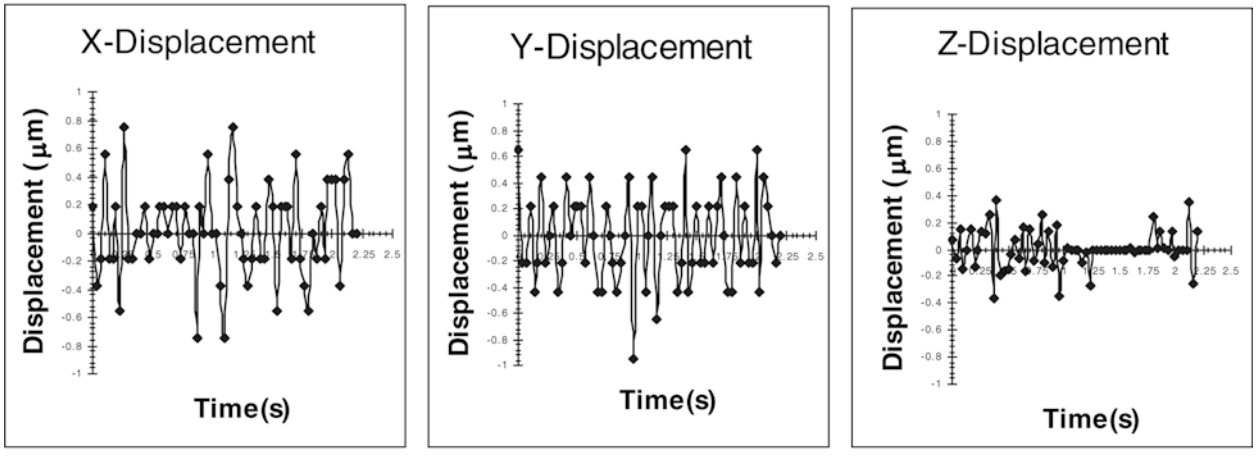

(b)

Fig. 8a, b. Manual tracking of the Brownian motion of a single 200-nm particle suspended in water at 293K. **a** The history of three-dimensional locations over 67 imaging frames recorded for the duration of 2.23 s. **b** The history of its x–y–z directional displacements

coefficients, as well as MSD. The measured MSD values of $\langle \Delta x^2 \rangle$ and $\langle \Delta y^2 \rangle$ compare well with the theoretical predictions. However, the measured values of $\langle \Delta z^2 \rangle$ are rather substantially underestimated compared to the predictions, and the resulting measured $\langle \Delta r^2 \rangle$ slightly but noticeably deviates from the theory. The theoretical diffusion coefficient $D_{||}$ is calculated based on either of the identical MSD in the x and y directions, while the experimental $D_{||}$ is determined from the average of the measured x and y MSD values. Their comparison is seen to be in good agreement with each other. The measured normal diffusion coefficient $D_{\perp}$, however, is seen to be about one-third of the theoretically estimated value.

The z directional underestimation is persistent and is believed to be the result of the physical inadequacy and limitation of the near-wall hindrance theory (Brenner 1961) for the present experimental conditions. Brenner's analysis takes into consideration only the hydrodynamic interaction between a single sphere and the wall[9]. The

[9]Meiners and Quake (1999) attempted a direct measurement of hydrodynamic interaction between two spherical colloid particles, ranging from 3.1 μm to 9.8 μm, two order of magnitudes larger than the present nanoparticles, suspended by optical tweezers in an external potential. However, they measured the cross-correlations of only two-dimensional motions of particles without accounting for the near-wall hindrance.

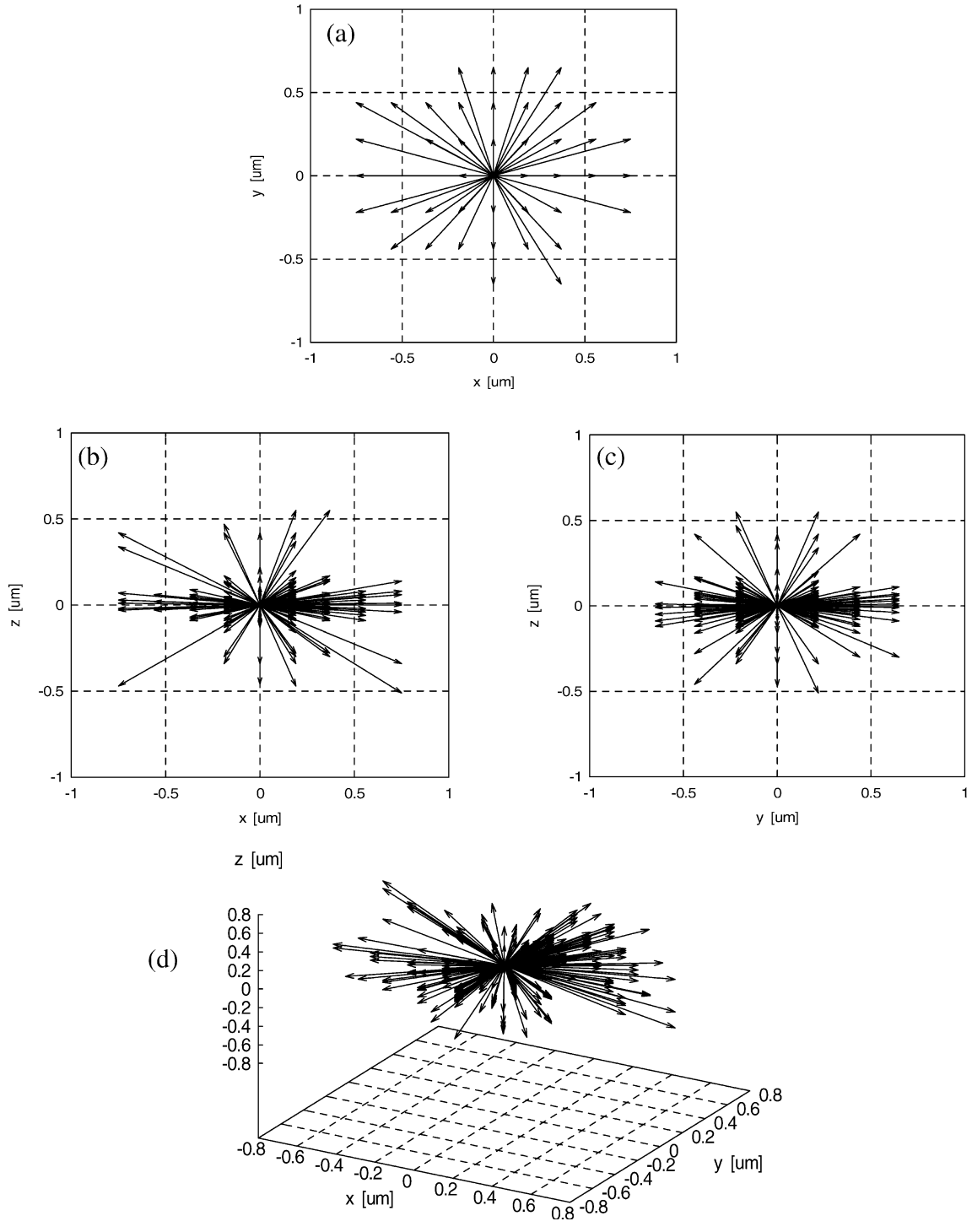

Fig. 9a–d. Brownian diffusive displacements for multiple 200-nm particles tracked by the neural network model: the anisotropic displacements in the lateral x–y plane (**a**); the normally quenched displacements in the line-of-sight x–z, y–z planes (**b**, **c**); and the three-dimensional displacements (**d**)

resulting correction coefficient for the normal diffusion, ξ in Eq. 10, does not take into account additional hindering effects, such as electrostatic and electro-osmotic forces between them. It is the authors' conjecture that the formation of an electronic double layer (EDL) on the cover glass surface plays a key part here. When the cover glass comes into contact with an aqueous solution, the surface hydrolyzes to form the silanol surface group and the glass surface is negatively charged to SiO^-. The negatively charged glass surface attracts the positive hydrogen ions from the weakly ionized water to form EDL (Probstein 1994). The EDL thickness or the so-called Debye length, ranges from 10 to 100 nm, depending on the ionic concentration of the solution (Kim et al. 2002). This range is well within the penetration depth z_p and the measured displacements can be altered by the electro-osmotic

Table 1. Comparison of theoretical predictions with measured data for Brownian motion of 200-nm particles in water at 20°C for a specified time interval of 33 ms: free diffusion coefficient (D), hindered elementary (normal: $D_\perp$, lateral: $D_\parallel$), and hindered bulk diffusion coefficients (D_O)

Parameters	Units	Theory	Neural-network-based multiple particle tracking data	Single-particle manual tracking data
Mean square displacement (MSD)				
$<\Delta r^2>$	μm^2	0.2753	0.2517	0.2278
$<\Delta x^2>$		0.1022	0.1069	0.1024
$<\Delta y^2>$		0.1022	0.1234	0.1008
$<\Delta z^2>$		0.0709	0.0214	0.0246
Brownian diffusivity				
D	$\mu m^2/s$	2.1451	–	–
D_O		1.3765	1.2585	1.1390
$D_\parallel$		1.5330	1.7273	1.5240
$D_\perp$		1.0635	0.3210	0.3690
Mean displacement				
$<\Delta r>$	μm	0	0.0208	0.0244
$<\Delta x>$		0	−0.0146	0.0167
$<\Delta y>$		0	0.0145	−0.0176
$<\Delta z>$		0	0.0033	0.0030
Mean of absolute displacement				
$<\lvert\Delta r\rvert>$	μm	0.5247	0.4548	0.3791
$<\lvert\Delta x\rvert>$		0.3197	0.2987	0.2437
$<\lvert\Delta y\rvert>$		0.3197	0.3339	0.2761
$<\lvert\Delta z\rvert>$		0.2663	0.0786	0.0901

interactions. Consequently, the negatively charged $COOH^-$ group of the fluorescence tracer particles may be repelled away from the surface, and this can act to significantly hinder the diffusion motion beyond the hydrodynamic hindrance, resulting in substantially lower MSD measurements in the normal direction than in Brenner's theory. It is uncertain, however, whether the pertinent effect is the sole reason for the excessive near-wall hindering or not. Certainly, more elaborate future investigation will be necessary to examine this conjecture.

The mean particle displacement $\langle\Delta r\rangle$, as well as $\langle\Delta x\rangle$, $\langle\Delta y\rangle$, and $\langle\Delta z\rangle$ should be ideally zero because of the spherically symmetric random nature of the Brownian motion. The corresponding experimental data strongly manifests this random nature, showing extremely small values. The measured mean absolute displacements $\left(\langle|\Delta r|\rangle \equiv \sum_i^N |\Delta r|_i \Big/ N\right)$ show acceptable agreement with the theory for both the single and multiple particle results. Since no theoretical estimation is available, the square root of the MSD is used to approximately predict the mean of the absolute displacements. The $\langle|\Delta z|\rangle$ measurement shows underestimation that is persistent with the previous discussions.

Finally, a comment should be made regarding the various measurement uncertainties associated with the R-TIRFM system. More detailed discussions are presented in the Appendix. Measurement of I_N by Eq. 5 involves a number of errors because of background noise in the image. The major errors are attributed to the background fluorescence and the lateral scattering of the excitation light by the neighboring particles. These errors are largely eliminated by using a low concentration of the fluorophore in water (0.001% by volume at present) and keeping the penetration depth minimal to improve the image contrast. Another important uncertainty occurs in estimating z_p because of the incident angle uncertainty, and the inaccurate refractive indices of the cover glass, the emersion oil, and the fluorophore solution. Additional errors can be caused by the uncertainty of the illumination light intensity at the surface because of the micro/nanoscale non-uniformities of the laser illumination. Indeed, some illumination non-uniformities are substantial, as demonstrated in Fig. 3b. However, most particles are fluctuating locally within the region of fairly uniform illumination intensity so that their images are minimally biased by the observed large-scale spatial non-uniformities. As for the temporal variations in the laser intensity, all experiments were performed after the laser beam was stabilized and fluctuations were within 0.1 mW. Furthermore, the intensity variation during such a relatively short imaging period, a maximum of 4 s, should be negligibly small.

4 Conclusive remarks

A novel three-dimensional ratiometric particle tracking technique has been developed and applied to examine the hindered Brownian diffusion of 200-nm fluorescent particles within a penetration depth of z_p=272 nm from the interface given at θ_i=62°. Three-dimensional particle displacements are analyzed using a robust neural network model to identify particle pairs across imaging frames. The technique is likely considered as the first of its kind to tag and track nanoparticles in a full three-dimensional way with unprecedented nanometer spatial resolution. The overall measurement uncertainties are estimated as ±71.7 nm both in the x and y direction, and ±29.38 nm in the z direction. The measured Brownian diffusion behavior show fairly impressive agreement with the near-wall

hindrance theory in the lateral x–y plane, but the measured diffusion coefficient in the z direction is approximately one-third of the theoretical result. Noting that the theory is based on the consideration of the pure hydrodynamic interaction of a single particle with the wall, the authors propose to further examine the near-wall hindrance model by additionally incorporating non-hydrodynamic effects such as electrostatic and electro-osmotic forces that may be prevalent within the penetration depth of the evanescent wave field.

5 Uncertainty analyses

Experimental uncertainties have been estimated based on a single-sample experiment, where only one measurement is made for each point (Kline and McClintock 1953). Four pertinent uncertainties are presented: (1) uncertainty for incident ray angle θ; (2) uncertainty for the lateral (x–y) Brownian displacement measurements Δx or Δy; (3) uncertainty for the penetration depth z_p; and (4) uncertainty for the z directional relative displacement Δh.

5.1 Uncertainty for incident ray angle

The evanescent wave rim radius at the back-focal plane of the lens, R (http://www.olympusmicro.com), is given as $R=fn\sin\theta$, where the focal length of the TIRF objective lens f=3 mm and the refractive index of the incident cover glass medium n=1.515. A measurement function for the incident ray angle is defined as $\sin\theta=R/fn=g(R, f, n)$. The Kline-McClintock analysis (Fox et al. 2004) for uncertainty w_g gives:

$$\begin{aligned} w_g &= \pm\left[\left(\frac{\partial g}{\partial R}w_R\right)^2+\left(\frac{\partial g}{\partial f}w_f\right)^2+\left(\frac{\partial g}{\partial n}w_n\right)^2\right]^{\frac{1}{2}} \\ &= \pm\left[\left(\frac{w_R}{R}g\right)^2+\left(-\frac{w_f}{f}g\right)^2+\left(-\frac{w_n}{n}g\right)^2\right]^{\frac{1}{2}} \\ &= \pm\left[\left(\frac{w_R}{fn}\right)^2+\left(\frac{w_f\sin\theta}{f}\right)^2+\left(\frac{w_n\sin\theta}{n}\right)^2\right]^{\frac{1}{2}} \end{aligned} \tag{18}$$

where w_R, w_f, and w_n are the uncertainties associated with the individual parameters of R, f, and n. Per the resolution limit provided by Olympus Inc., w_R=±0.025 mm, and both the focal length uncertainty, w_f, and the refractive index uncertainty, w_n, are assumed to be negligibly small. For the incident angle of 62°, the resulting uncertainty is calculated as $w_\theta = \pm 0.315^\circ$ after a conversion based on $w_\theta=\sin^{-1}(w_g)$.

5.2 Uncertainty for the lateral (x–y) Brownian displacement measurements

A reasonable estimate of the measurement uncertainty due to random error is plus or minus half of the smallest scale division, equivalent to 1 pixel, of the CCD camera. By taking the average pixel displacements as 3 pixel, the lateral displacement uncertainty is estimated to be $w_x = w_y = \pm 0.5$ pixel $\cong \pm 71.7$ nm.

5.3 Uncertainty for the penetration depth z_p

Considering Eq. 2:

$$z_p = \frac{\lambda_0}{4\pi}\left(n_i^2\sin^2\theta - n_t^2\right)^{-\frac{1}{2}}$$

the uncertainty equation for z_p is given as:

$$\begin{aligned} w_{z_p} = \pm\Bigg[&\left(\frac{\partial z_p}{\partial\lambda_0}w_{\lambda_0}\right)^2+\left(\frac{\partial z_p}{\partial n_i}w_{n_i}\right)^2 \\ &+\left(\frac{\partial z_p}{\partial n_t}w_{n_t}\right)^2+\left(\frac{\partial z_p}{\partial\theta}w_\theta\right)^2\Bigg]^{\frac{1}{2}} \end{aligned} \tag{19}$$

where the optical blue filter for the laser beam has a bandwidth of $w_{\lambda_0} = \pm 2$ nm, $w_\theta = \pm 0.315^\circ$ (first section of Appendix), and variations of refractive indices are neglected, i.e., $w_{n_i} = w_{n_t} = 0$. The measurement uncertainty of z_p shows a significant increase with the incident ray angle θ approaching the critical value of θ_c=61.38° (Fig. 10). For example, the penetration depth uncertainty is estimated as $w_{z_p} = \pm 4.75$ nm for θ=65°, but increases to $w_{z_p} = \pm 69.47$ nm for θ=62°.

5.4 Uncertainty for the line-of-sight (z) Brownian displacement measurements

The uncertainty of Δh can be estimated by applying the uncertainty analysis to the ratiometric intensity relation given in Eq. 6 as:

$$RaInt = \frac{I_N^1(h_1,\ R,\ c)}{I_N^2(h_2,\ R,\ c)} = \mathrm{e}^{\left(-\frac{\Delta h}{z_p}\right)}$$

or equivalently:

$$\Delta h = -z_p\ln(RaInt) = z_p\left[\ln\left(I_N^2\right)-\ln\left(I_N^1\right)\right] \tag{6a}$$

Thus, the uncertainty equation is obtained as:

$$w_{\Delta h} = \pm\left[\left(\frac{\partial\Delta h}{\partial z_p}w_{z_p}\right)^2+\left(\frac{\partial\Delta h}{\partial I_N^2}w_{I_N^2}\right)^2+\left(\frac{\partial\Delta h}{\partial I_N^1}w_{I_N^1}\right)^2\right]^{\frac{1}{2}} \tag{20}$$

The elementary uncertainties of $w_{I_N^1}$ and $w_{I_N^2}$ may be estimated from the statistical nature of the measured data. A statistical analysis was conducted for the particle tracking data for θ_i=62° and the resulting statistical properties are summarized in terms of the pixel gray level, as shown in Table 2. Thus, the elementary uncertainties for the image intensities is assumed to be equal to the width of a 95% confidence interval, i.e., $w_{I_N^1} = w_{I_N^2} = \pm 10.6835$ (pixel equivalency), the reference particle image intensity I_N^2 is assumed to have the maximum intensity of 220, and the arbitrary particle image intensity I_N^1 is assumed to have the average intensity of 165.94. Substituting these values into Eq. 20, the overall uncertainty for the z location measurements is estimated as $w_{\Delta h} = \pm 29.38$ nm for θ=62°. This R-TIRFM uncertainty also decreases with increasing incident ray angle,

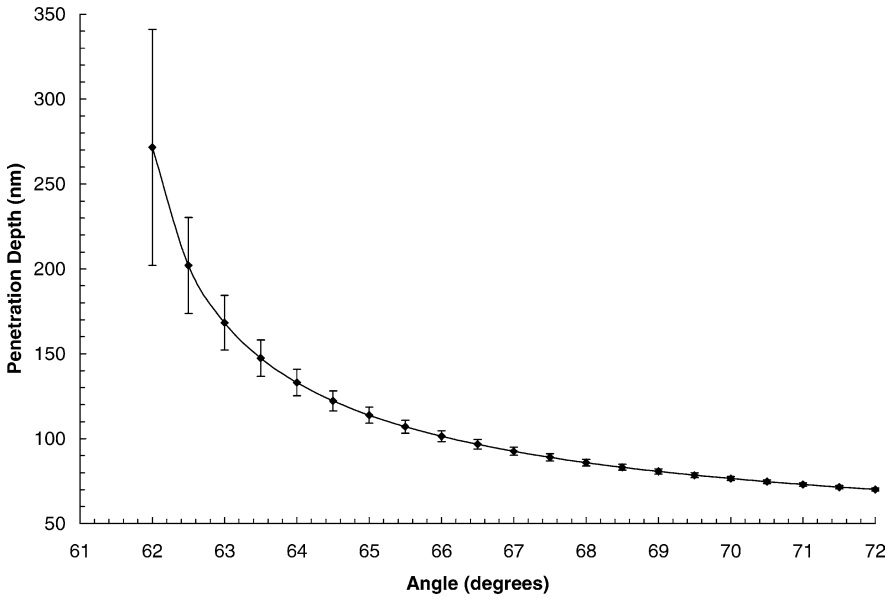

Fig. 10. Calculated uncertainty for the penetration depth (z_p) for different incident angles (θ) with θ_c=61.38° for the glass–water interface (n_i=1.515 for glass, n_t=1.33 for water)

Table 2. Statistical properties of the analysis conducted for the particle tracking data for θ_i=62°

Mean gray level	165.9404
Standard error	5.40689
Median	210
Mode	220
Standard deviation	66.44097
Sample variance	4414.403
Kurtosis	−1.02024
Skewness	−0.77834
Range	187
Minimum	33
Maximum	220
Sum	25057
Count	151
Largest (1)	220
Smallest (1)	33
Confidence level (95.0%)	10.6835

depicting a similar trend of the penetration depth uncertainty.

References

Axelrod D, Burghardt TP, Thompson NL (1984) Total internal reflection fluorescence (in biophysics). Annu Rev Biophys Bio 13:247–268

Axelrod D, Hellen EH, Fulbright RM (1992) Total internal reflection fluorescence. In: Lakowicz J (ed) Topics in fluorescence spectroscopy: principles and applications, vol 3: biochemical applications. Plenum Press, New York, pp 289–343

Banerjee A, Chon C, Kihm KD (2003) Nanoparticle tracking using TIRFM imaging. In: Photogallery of the ASME international mechanical engineering congress and exposition (IMECE 2003), Washington, DC, November 2003

Batchelor GK (1975) Brownian diffusion of particles with hydrodynamic interaction. J Fluid Mech 74:1-29

Bevan MA, Prieve DC (2000) Hindered diffusion of colloidal particles very near to a wall: revisited. J Chem Phys 113(3):1228–1236

Born M, Wolf E (1980) Principles of optics, 6th edn. Cambridge University Press, Cambridge, pp 47–51

Brenner H (1961) The slow motion of a sphere through a viscous fluid towards a plane surface. Chem Eng Sci 16:242–251

Brown R (1828) A brief account of microscopical observations made in the months of June, July, and August, 1827, on the particles contained in the pollen of plants; and on the general existence of active molecules in organic and inorganic bodies. Phil Mag 4:161–173

Burghart TP, Thompson NL (1984) Effects of planar dielectric interfaces on fluorescence emission and detection. Biophys J 46:729–737

Deen WM (1998) Analysis of transport phenomena. Oxford University Press, New York, pp 59–63

Denk W, Strickler JH, Webb WW (1990) Two-photon laser scanning fluorescence microscopy. Science 248:73–76

Dufresne ER, Squires TM, Brenner MP, Grier DG (2000) Hydrodynamic coupling of two Brownian spheres to a planar surface. Phys Rev Lett 85:3317–3320

Einstein A (1905) Über die von der molekularkinetischen Theorie der Wärme geforderte Bewegung von in ruhenden Flüssigkeiten suspendierten Teilchen. Ann Physik 17**:** 549

Einstein A (1956) Investigations on the theory of Brownian movement. Dover, New York

Fox RW, McDonald AT, Pritchard PJ (2004) Introduction to fluid mechanics, 6th edn. Wiley, Hoboken, New Jersey, pp 755–761

Goldman AJ, Cox RG, Brenner H (1967) Slow viscous motion of a sphere parallel to a plane. I: motion through a quiescent fluid. Chem Eng Sci 22:637–651

Goos VF, Hanchen H (1947) Ein neuer und fundamentaler versuch zur totalreflexion. Ann Physik 1:333–346

Hecht E (2002) Optics, 4th edn. Addison-Wesley, Reading, Massachusetts, pp 124–127

Hellen EH, Axelrod D (1986) Fluorescence emission at dielectric and metal film interfaces. J Opt Soc Am B 4:337–350

Hosoda M, Sakai K, Takagi K (1998) Measurement of anisotropic Brownian motion near an interface by evanescent light-scattering spectroscopy. Phys Rev E 58(5):6275–6280

Ingenhousz J (1779) Experiments on vegetables, discovering their great power of purifying the common air in sunshine, and of injuring it in the shade or at night. In: Marshall HL, Herbert SK (1952) A source book in chemistry: 1400–1900. Harvard University Press, Cambridge, Massachusetts

Inoue S (1987) Video microscopy. Plenum Press, New York

Ishijima A, Yanagida T (2001) Single molecule nanobioscience. Trends in Biochem Sci 26:438–444

Jin S, Huang P, Park J, Yoo JY, Breuer KS (2003) Near-surface velocimetry using evanescent wave illumination. In: Proceedings of the ASME international mechanical engineering congress and exposition (IMECE 2003), Washington, DC, November 2003, paper 44015

Kim MJ, Beskok A, Kihm KD (2002) Electro-osmosis-driven microchannel flows: a comparative study of microscopic particle image velocimetry measurements and numerical simulations. Exp Fluids 33:170–180

Kim S, Karrila SJ (1991) Microhydrodynamics: principles and selected applications. Butterworth-Heinemann, Stoineham, Massachusetts
Kline SJ, McClintock FA (1953) Describing uncertainties in single-sample experiments. Mech Eng 75(1): 3–9
Kohonen T (1995) Self-organizing maps. Springer, Berlin Heidelberg, New York
Kohonen T, Kaski S, Lappalainen H (1994) Self-organized formation of various invariant-feature filters in the adaptive subspace SOM. Neural Comput 9:1321–44
de Lange F, Cambi A, Huijbens R, de Bakker B, Rensen W, Garcia-Parajo M, van Hulst N, Figor CG (2001) Cell biology beyond the diffraction limit: near-field scanning optical microscopy. J Cell Sci 114:4153–4160

Meiners J-C, Quake SR (1999) Direct measurement of hydrodynamic cross correlations between two particles in an external potential. Phys Rev Lett 82(10):2211–2214
Molecular Probes (2004) Personal communications, Molecular Probes Inc., Eugene, Oregon
Nakroshis P, Amoroso M, Legere J, Smith C (2003) Measuring Boltzmann's constant using video microscopy of Brownian motion. Am J Phys 71(6):568–573
Okamoto K, Hassan YA, Schmidl WD (1995) New tracking algorithm for particle image velocimetry. Exp Fluids 19:342–347
Okamoto K, Nishio S, Kobayashi T, Saga T (1997) Standard images for particle imaging velocimetry. In: Proceedings of the 2nd international workshop on particle image velocimetry (PIV'97), Fukui, Japan, July 1997, pp 229–236
Park JW, Choi CK, Kihm KD (2004) Optically slices micro-PIV using confocal laser scanning microscopy (CLSM). Exp Fluids 37:105–119
Pawley JB (1995) Handbook of biological confocal microscopy, 2nd edn. Plenum Press, New York
Prieve DC (1999) Measurement of colloidal forces with TIRM. Adv Colloid Interfac 82:93–125
Probstein RF (1994) Physicochemical hydrodynamics. Wiley, New York
Rohrbach A (2000) Observing secretory granules with a multiangle evanescent wave microscope. Biophys J 78:2641–2654
Sako Y, Minoghchi S, Uyemura T (2000) Single-molecule imaging of EGFR signaling on the surface of living cells. Nat Cell Biol 2:168–172
Sako Y, Yanagida T (2003) Single-molecule visualization in cell biology. Nat Rev Mol Cell Bio September supplement SS1-SS5
Salmon R, Robbins C, Forinash K (2002) Brownian motion using video capture. Eur J Phys 23(3):235-253
Schatzel K, Neumann WG, Muller J, Materzok B (1992) Optical tracking of Brownian particles. Appl Optics 31:770–778
Shlesinger MF, Klafter J, Zumofen G (1999) Above, below and beyond Brownian motion. Am J Phys 67:1253–1259
Stelzer EHK, Lindek S (1994) Fundamental reduction of the observation volume in far-field light microscopy by detection orthogonal to the illumination axis: confocal theta microscopy. Opt Commun 111:536–547
Takagi T, Okamoto K (2001) Particle tracking velocimetry by network model. In: Proceedings of the 3rd Pacific symposium on flow visualization and image processing (PSFVIP-3), Maui, Hawaii, March, conference CD-ROM
Weiss S (2000) Measuring conformational dynamics of biomolecules by single molecule fluorescence spectroscopy. Nat Struct Biol 7:724–729
Xie S (2001) Single-molecule approach to enzymology. Single Mol 2:229–236
Zettner CM, Yoda M (2003) Particle velocity field measurements in a near-wall flow using evanescent wave illumination. Exp Fluids 34:115–121